

CrossMark  
click for updatesCite this: *Catal. Sci. Technol.*, 2015,  
5, 2985

# The performance and mechanism of Ag-doped CeO<sub>2</sub>/TiO<sub>2</sub> catalysts in the catalytic oxidation of gaseous elemental mercury

Songjian Zhao, Zan Qu, Naiqiang Yan,\* Zhen Li, Haomiao Xu, Jian Mei and Fuquan Quan

To improve the ability of CeO<sub>2</sub>/TiO<sub>2</sub> catalysts to catalyze the oxidation of gaseous elemental mercury, silver was introduced. Doping with Ag can significantly enhance the Hg<sup>0</sup> oxidation ability of CeO<sub>2</sub>/TiO<sub>2</sub>. In addition, the temperature window was widened (from 150 to 450 °C). The catalysts were characterized by TEM, XRD, XPS and H<sub>2</sub>-TPR. The results indicated that silver nanoparticles can be loaded on the TiO<sub>2</sub> support. The catalysts had better crystallization and higher redox ability after addition of silver. Silver existed mostly in its metallic state, which can keep Ce in a higher Ce(IV) state. HCl was oxidized into active Cl by CeO<sub>2</sub> and then was adsorbed on the silver nanoparticles. In addition to the HCl and Hg<sup>0</sup> breakthrough experiments, a Hg<sup>0</sup> desorption experiment and a Cl<sub>2</sub> yield experiment were conducted to study the catalytic mechanisms of elemental mercury oxidation over various temperature ranges; these experiments indicated that the reaction followed the Langmuir–Hinshelwood mechanism at low temperature, and the Eley–Rideal mechanism and homogeneous gas-phase reaction at high temperature. Furthermore, a mercury valence state change experiment was performed, which indicated that HCl was the major catalytic oxidization component.

Received 6th January 2015,  
Accepted 23rd March 2015

DOI: 10.1039/c4cy01745e

www.rsc.org/catalysis

## 1. Introduction

Elemental mercury emitted into the atmosphere during the process of coal combustion pollutes the air and causes adverse effects on the health of humans.<sup>1</sup> Therefore, many measures have been taken to reduce mercury emissions in recent decades. The U.S. EPA updated the emission limits for new power plants under the Mercury and Air Toxics Standards (MATS) on March 28, 2013.<sup>2</sup> In October 2013, a new international convention to control mercury emissions named the Minamata Convention on Mercury was signed by most countries, which was a response to the issue of global mercury pollution.<sup>3</sup>

Mercury exists in three forms in coal-fired flue gas: elemental mercury (Hg<sup>0</sup>), oxidized mercury (Hg<sup>2+</sup>) and particulate-bound mercury (Hg<sup>p</sup>). Hg<sup>2+</sup> and Hg<sup>p</sup> are relatively easy to remove from flue gas by using typical air pollution control devices. However, elemental mercury (Hg<sup>0</sup>) is difficult to remove from flue gas due to its high equilibrium volatility and low solubility in water.<sup>4</sup> Therefore, it is necessary to develop effective technologies to remove Hg<sup>0</sup>. The catalytic conversion of Hg<sup>0</sup> to its oxidized form over catalysts

subsequently captured by existing air pollution control devices is considered to be an effective method for Hg<sup>0</sup> emission control.

In recent years, a great deal of research into metal oxide catalysts has been extensively conducted to develop effective Hg<sup>0</sup> oxidation technologies.<sup>5–8</sup> CeO<sub>2</sub> was heralded as an effective catalyst due to its large oxygen storage capacity and unique redox couple Ce<sup>3+</sup>/Ce<sup>4+</sup> with the ability to shift between CeO<sub>2</sub> and Ce<sub>2</sub>O<sub>3</sub> under oxidizing and reducing conditions, respectively, which was used for the catalytic oxidation of elemental mercury.<sup>9,10</sup> However, the appropriate temperature window for Hg<sup>0</sup> oxidation is not wide, and the efficiency of Hg<sup>0</sup> oxidation over CeO<sub>2</sub>–TiO<sub>2</sub> catalysts depends on the HCl concentration in the flue gas.<sup>11</sup>

Silver has long been recognized as an effective catalytic component and has been shown to facilitate the redox process.<sup>12,13</sup> Delaigle *et al.* used V<sub>2</sub>O<sub>5</sub>/TiO<sub>2</sub> catalysts doped with silver in the oxidation of chlorobenzene, which maintained vanadium in a higher oxidation state and induced higher catalytic performance.<sup>14</sup> Ma *et al.* prepared Ag/CeO<sub>2</sub> nanosphere catalysts for formaldehyde oxidation and found that synergistic interactions might exist between Ag and CeO<sub>2</sub> nanospheres, and the presence of silver could facilitate the activation of surface chemisorbed oxygen, which mainly contributed to HCHO oxidation.<sup>15</sup> In addition, silver has been recognized as an efficient adsorbent for the capture of

School of Environmental Science and Engineering, Shanghai Jiao Tong University, 800 Dong Chuan Road, Shanghai, 200240, PR China. E-mail: nqyan@sjtu.edu.cn; Fax: +86 21 54745591; Tel: +86 21 54745591

$\text{Hg}^0$  at low temperatures through an amalgamation mechanism. Thus, the combination of Ag and Ce may be feasible in enhancing the  $\text{Hg}^0$  catalytic efficiency and widening the temperature window of the reaction.

In the present study, catalysts were prepared using a room-temperature impregnation method. The physical and chemical properties of the catalysts, as well as the  $\text{Hg}^0$  oxidation efficiency, were investigated. Furthermore, the catalytic mechanisms involved in improving the efficiency at various temperatures were discussed.

## 2. Experimental section

### 2.1 Materials

Commercially available  $\text{TiO}_2$  powder (Degussa P25) was mainly used as the carrier of the various catalysts. It was the standard material used for all purposes and contained anatase and rutile phases in a ratio of approximately 3:1. All chemicals used for catalysts' preparation were of analytical grade and were purchased from Sigma-Aldrich Co. and Sino-pharm Chemical Reagent Co. The standardized  $\text{SO}_2$  (10 000 ppm), NO (5000 ppm) and HCl (2000 ppm and 5%) gases were provided by Dalian Date Gas Co.

### 2.2 Preparation of catalysts

Catalysts were prepared by an impregnation method, which included  $\text{CeO}_2\text{-TiO}_2$ ,  $\text{Ag-TiO}_2$  and  $\text{Ag-CeO}_2\text{-TiO}_2$ . An appropriate amount of P25 was added to a  $(\text{NH}_4)_2\text{Ce}(\text{NO}_3)_6$  solution and the mixture was stirred for 1 h, which was marked as the "A" solution. Polyvinylpyrrolidone (PVP) was dissolved in water, and the  $\text{AgNO}_3$  precursor was then added. The mixed solution was stirred for 6 h at room temperature and was marked as the "B" solution. The B solution was added dropwise into the A solution and the mixed solution was stirred constantly for 2 h. The mixed solution was then evaporated and dried using a rotary evaporation apparatus and was then finally calcined in a muffle furnace (5 h, 500 °C). The  $\text{CeO}_2\text{-TiO}_2$ ,  $\text{Ag-TiO}_2$  and  $\text{Ag-CeO}_2\text{-TiO}_2$  catalysts were labeled as Ce-Ti, Ag-Ti and Ag-Ce-Ti. The proportion of Ce and Ag to  $\text{TiO}_2$  is based on the atomic percentages, such that  $\text{Ce}(x\%)\text{-Ti}$  represents the  $\text{CeO}_2/\text{TiO}_2$  mole ratio, and 1% was omitted.

### 2.3 Catalytic activity evaluation

The catalytic activity was evaluated using a simulated gas preparation system and a catalytic reaction device, in which a cold vapor atomic absorption spectrometer (CVAAS) and an online data acquisition system were employed. The simulated gas system and the catalytic reaction device included eight mass flow controllers which were used to prepare the simulated flue gas compositions and a fixed-bed reactor (a quartz tube with an inner diameter of 6 mm and a tube type resistance furnace). The catalyst (40–60 mesh particles) was added to the quartz tube and fixed with quartz wool.  $\text{Hg}^0$  vapor was prepared from the  $\text{Hg}^0$  permeation unit and was blended

with the gases before they entered the reactor. The concentration of elemental mercury in the gas was analyzed using a mercury analyzer (CVAAS SG-921).

At the beginning of each test, the gas containing elemental mercury was first passed through the bypass without a catalyst and was subsequently sent to the CVAAS to determine the baseline. When the concentration of elemental mercury remained within  $\pm 5\%$  for more than 30 min, the gas was diverted to the fixed-bed reactor with catalysts. 5 ppm HCl was passed to estimate the oxidation efficiency of  $\text{Hg}^0$  until the catalysts were saturated. The gas flow rate was  $30 \text{ L h}^{-1}$ , corresponding to a space velocity (SV) of  $4.26 \times 10^5 \text{ h}^{-1}$ . Nitrogen was used as the carrier gas, and the oxygen content was 4%.

Because the catalysts were first saturated in approximately  $300 \mu\text{g m}^{-3} \text{Hg}^0$  plus  $\text{N}_2$  and  $\text{O}_2$  gas flow, the decrease in  $\text{Hg}^0$  concentration across the catalysts after passing HCl was attributed to  $\text{Hg}^0$  oxidation. Besides, an Online Mercury Emissions Monitoring System (3300 RS) proved that  $\text{Hg}^0$  in the flue gas was oxidized by the catalysts. Furthermore, mercury on the surface of the catalysts was analyzed using a RA-915+ mercury analyzer (Lumex, Russia) equipped with a liquid analysis unit and a solid pyrolysis unit (RP-91C), and it was found that the concentration of  $\text{Hg}^0$  on the surface of the catalysts was little, and only a little amount of  $\text{Hg}^{2+}$  species existed. Accordingly, the definition of  $\text{Hg}^0$  oxidation efficiency ( $E_{\text{oxi}}$ ) over catalysts is as follows:

$$E_{\text{oxi}} (\%) = \frac{\Delta \text{Hg}^0}{\text{Hg}_{\text{in}}^0} = \frac{\text{Hg}_{\text{in}}^0 - \text{Hg}_{\text{out}}^0}{\text{Hg}_{\text{in}}^0}$$

### 2.4 Characterization of the catalysts

The XRD patterns of the catalysts were obtained with an X-ray diffractometer (APLX-DUO, BRUKER, Germany) using  $\text{Cu K}\alpha$  radiation (40 kV and 20 mA). The microstructure of the catalysts was analyzed by transmission electron microscopy (TEM). The sample was dispersed in ethanol under strong sonication before analysis.  $\text{H}_2\text{-TPR}$  experiments were performed on a Chemisorp TPx 2920 instrument. The catalysts were degassed at 200 °C for 3 h under Ar atmosphere before the  $\text{H}_2\text{-TPR}$  test. The reducing gas was 10%  $\text{H}_2/\text{Ar}$ . X-ray photoelectron spectroscopy (XPS) measurement was conducted using an AXIS UltraDLD (Shimadzu-Kratos) spectrometer with  $\text{Al K}\alpha$  as the excitation source. The C 1s line at 284.8 eV was taken as a reference for binding energy calibration. The  $\text{Cl}_2$  produced by Deacon reaction was monitored *in situ* using a UV/vis spectrometer equipped with an optical fiber for UV-beam transmission and a detector in the range of 200–800 nm. The maximum UV absorbance of chlorine is at approximately 330 nm. The valence state change of mercury was analyzed by an Online Mercury Emissions Monitoring System (3300 RS). The temperature programmed desorption curves of  $\text{Hg}^0$  was obtained as follows: a known amount of the catalyst was placed in the catalytic reaction device with  $\text{N}_2 + 4\% \text{O}_2$  at  $30 \text{ L h}^{-1}$  and 100 °C to adsorb

mercury for 2 h; afterwards, the flow of oxygen was stopped, and the Hg signal curve was recorded at  $2\text{ }^{\circ}\text{C min}^{-1}$  until it reached  $450\text{ }^{\circ}\text{C}$  under nitrogen.

### 3. Results and discussion

#### 3.1 The effect of silver on the catalytic oxidation of $\text{Hg}^0$

Fig. 1 shows the comparison of  $\text{Hg}^0$  catalytic oxidation efficiencies over Ce-Ti and Ag-Ce-Ti with various temperatures at  $4.26 \times 10^5\text{ h}^{-1}$  space velocity. Fig. 1 shows that the catalytic efficiency of Ce-Ti and Ag-Ce-Ti were both improved with the increase in temperature. Moreover, the  $\text{Hg}^0$  catalytic oxidation efficiency was significantly improved after addition of silver either at a low temperature or at a high temperature, which indicated that silver played an important role in the improvement of the catalytic performance the Ce-Ti catalyst. It was also found that Ag-Ce-Ti was an excellent catalyst and had a wide temperature window for  $\text{Hg}^0$  oxidation. Therefore, it was necessary to analyze the physical and chemical properties of the catalysts and the reaction mechanism.

#### 3.2 Physical and chemical characterization

Fig. 2 shows the XRD patterns of the various catalysts calcined at  $500\text{ }^{\circ}\text{C}$ . The anatase phase and the rutile phase of  $\text{TiO}_2$  are clearly seen in Fig. 2(b)–(d). The intensity of the peaks increased after addition of silver. This indicates that the catalysts had better crystallization, which was beneficial to the catalytic reaction.<sup>16,17</sup> The characteristic peaks of  $\text{CeO}_2$  are observed in Fig. 2(a), while these peaks are not obvious in Fig. 2(d), which manifested the uniform distribution of  $\text{CeO}_2$ . Additionally,  $\text{Ag}^0$  peaks could be observed in Fig. 2(c) and (d), indicating that metallic silver was present on the support.<sup>18–20</sup>

Fig. 3 shows the transmission electron microscopy (TEM) images of Ce-Ti and Ag-Ce-Ti. Fig. 3(a) shows that the Ce-Ti catalyst was composed of nanoparticles with sizes between 20 and 30 nm. Ceria could not be found on the surface of the catalyst, while EDS analysis results in Fig. 3(a) could

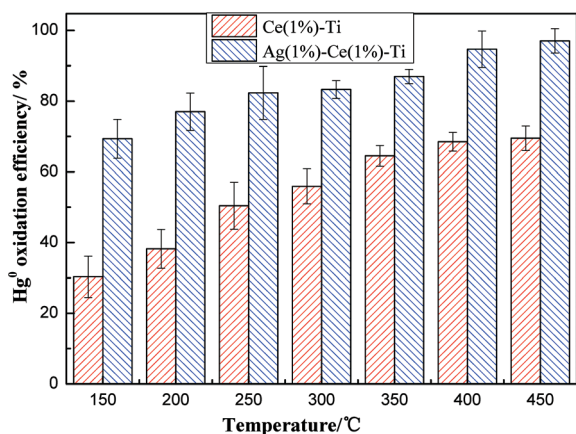


Fig. 1 Comparison of  $\text{Hg}^0$  catalytic oxidation efficiencies over Ce-Ti and Ag-Ce-Ti with various temperatures at  $4.26 \times 10^5\text{ h}^{-1}$  space velocity.

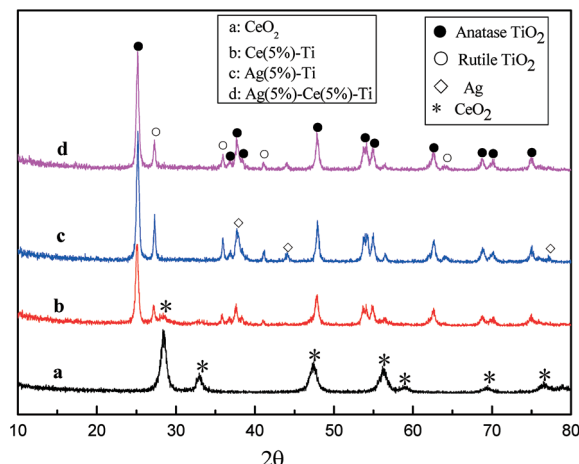


Fig. 2 XRD patterns of various catalysts calcined at  $500\text{ }^{\circ}\text{C}$ :  $\text{CeO}_2$  (a),  $\text{Ce}(5\%)\text{-Ti}$  (b),  $\text{Ag}(5\%)\text{-Ti}$  (c) and  $\text{Ag}(5\%)\text{-Ce}(5\%)\text{-Ti}$  (d).

prove the existence of ceria oxide on the carrier, which indicated that cerium atoms were well dispersed on  $\text{TiO}_2$ , or the low content referred to in the results of XRD. Many small particles are attached to the surfaces of  $\text{TiO}_2$ , as seen in Fig. 3(b), which are Ag nanoparticles. The size distribution of the silver nanoparticles was between 2–3 nm, indicating that the silver nanoparticles were evenly deposited on titania.

Fig. 4 shows the XPS spectra of Ce-Ti, Ag-Ce-Ti and Ag-Ce-Ti passed with 15 ppm HCl at various temperatures. It was reported that the  $\text{CeO}_2$  spectrum was composed of two multiplets (V and U), where V and U correspond to the spin-orbit split  $3d\ 5/2$  and  $3d\ 3/2$  core holes, respectively. The peaks referred to as v, v' and v'' are contributed by  $\text{CeO}_2$  and assigned to a mixture of  $\text{Ce(IV)} (3d^9\ 4f^2)\ \text{O} (2p^4)$ ,  $\text{Ce(IV)} (3d^9\ 4f^1)\ \text{O} (2p^5)$  and  $\text{Ce(IV)} (3d^9\ 4f^0)\ \text{O} (2p^6)$ , respectively. The same peak assignment is applied to u structures. The peaks  $v_0$  and  $v'$  are assigned to a mixture of  $\text{Ce(III)} (3d^9\ 4f^2)\ \text{O} (2p^5)$  and  $\text{Ce(III)} (3d^9\ 4f^1)\ \text{O} (2p^6)$ , respectively.<sup>9,21</sup> The Ce 3d spectra collected for Ag-Ce-Ti are shown in Fig. 4(a). It can be seen that Ce existed in a mixture of  $\text{Ce(IV)}$  and  $\text{Ce(III)}$  states, and the characteristic peaks shifted to higher binding energies after addition of silver, which indicated that the amount of  $\text{Ce(IV)}$  states was increased to be beneficial for the oxidation ability. When HCl was passed, the characteristic peaks slightly shifted to lower binding energies, manifesting the decrease in  $\text{Ce(IV)}$  states, which was due to the oxidation of HCl by  $\text{CeO}_2$ . In addition, the intensity of the peaks was not weakened, showing that HCl was not adsorbed on  $\text{CeO}_2$ .

The binding energies of Ag  $3d\ 5/2$  for Ag,  $\text{Ag}_2\text{O}$  and  $\text{AgO}$  were 368, 367.7 and 367.4 eV, respectively.<sup>22</sup> The XPS peaks of Ag 3d in Fig. 4(b) clearly show that silver is mostly present in the metallic state, which indicates that the particles on  $\text{TiO}_2$  are silver nanoparticles, referred to in the results of TEM. When HCl was passed, the intensity of the characteristic peaks was weakened and shifted to lower binding energies. It may be because the HCl adsorbed on the surface of Ag and  $\text{Ag}^0$  was oxidized to  $\text{Ag}^+$ . The peak of  $\text{Ag}_2\text{O}$  shifted to a lower binding energy, which may be due to HCl. With the

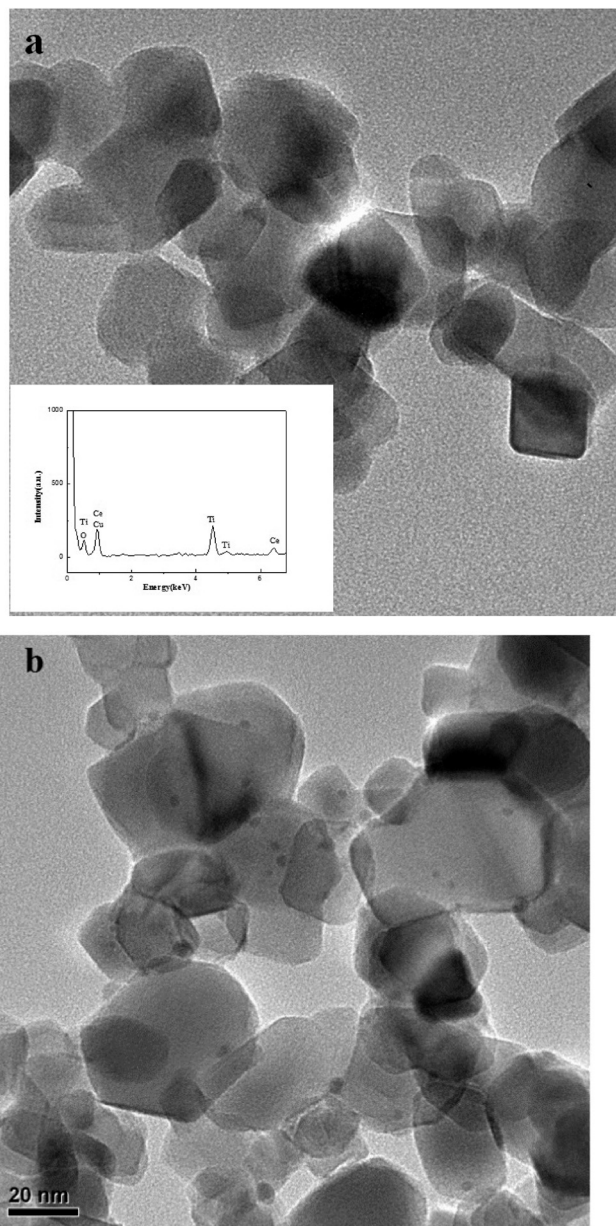


Fig. 3 Transmission electron microscopy (TEM) images of Ce-Ti and Ag-Ce-Ti: Ce-Ti (a) and Ag-Ce-Ti (b).

increase in temperature, the peaks' intensity was enhanced, indicating that the amount of adsorbed Cl was reduced.

The XPS Cl 2p spectra were investigated in this study, as shown in Fig. 4(c). Carrasco *et al.* reported that the Cl 2p spectra were resolved with three spin-orbit split doublets (Cl 2p 3/2 and Cl 2p 1/2) with binding energies for the Cl 2p 3/2 components at ~197, ~199 and ~200 eV.<sup>23,24</sup> In Fig. 4(c), the Cl 2p peaks centered at 197.2 and 200.2 eV correspond to ionic (Cl<sup>-</sup>) and covalent (-Cl) chlorine species, respectively, whereas the component at 198.3 eV is ascribed to the intermediate chlorine species (Cl\*). Fig. 4(c) shows that the chlorine species mainly existed as covalent (-Cl) chlorine species and intermediate chlorine species (Cl\*) at 200 °C, the covalent (-Cl) chlorine might be the HCl adsorbed on the surface

of the catalysts, and Cl\* might be the species that the adsorbed HCl oxidized. With the increase in temperature, covalent (-Cl) chlorine decreased, while the chlorine species (Cl\*) and the ionic species (Cl<sup>-</sup>) increased. It indicated that the HCl adsorption ability of the catalysts was poor with the increase in temperature. In addition, the catalysts' oxidation ability was enhanced at high temperatures, which can improve the yield of Cl\*. The appearance of ionic (Cl<sup>-</sup>) species may be due to the reduced chlorine species (Cl\*), oxidizing Ce<sup>3+</sup> and Ag<sup>0</sup> to Ce<sup>4+</sup> and Ag<sup>+</sup>. It can also be found that the peak intensities slowly decreased with increasing temperature, which may be because the adsorbed surface Cl was gradually removed.

The O 1s XPS spectrum is shown in Fig. 4(d). The common main peaks at 529.8 eV might be ascribed to lattice oxygen, and the peak at 531.4 eV could be attributed to surface chemisorbed oxygen. Furthermore, the positions of O 1s at 528.2 eV denoted nucleophilic species and those at 530.4 eV denoted electrophilic species, and the electrophilic oxygen could improve the oxidation step of metal ions from the low valence state to the high valence state.<sup>25</sup> Fig. 4(d) shows that there was no nucleophilic oxygen after addition of silver, which was beneficial for the oxidation ability of the catalysts. When HCl was passed at 200 °C, the characteristic peak of O shifted, which indicated that surface chemisorbed oxygen increased. The chemisorbed oxygen was beneficial for the oxidation reaction. With the increase in temperature, the chemisorbed oxygen was reduced, and the adsorption of oxygen on the surface of the catalysts at high temperatures became difficult.

The TPR profiles of the various catalysts are shown in Fig. 5. CeO<sub>2</sub> shows three peaks in Fig. 5(a). The peak that appeared at 410 °C corresponded to the reduction of surface oxygen and the peak at approximately 510 °C was related to the bulk oxygen,<sup>26</sup> while the peak at approximately 800 °C could be assigned to the lattice oxygen of CeO<sub>2</sub>.<sup>27</sup> When CeO<sub>2</sub> was loaded on TiO<sub>2</sub>, the characteristic peak of CeO<sub>2</sub> shifted to high temperature, which may have meant that CeO<sub>2</sub> was dispersed well on the carrier and there was an interaction between the two. The broad reduction peak starting from 100 °C and ending at about 180 °C could be attributed to the reduction of Ag<sub>2</sub>O on the support.<sup>28</sup> The peak of Ag-Ce-Ti that appeared at 120 °C in Fig. 5(d) could be attributed to the reduction of Ag<sub>2</sub>O, and the peak that appeared at about 200 °C may be related to the reduction of the surface oxygen of CeO<sub>2</sub> referred to in Fig. 5(b) and (c),<sup>15,29</sup> which was indicated by the fact that the peaks of CeO<sub>2</sub> shifted to low temperature after addition of silver. This showed that the redox ability of the catalysts was enhanced and was beneficial for the oxidation reaction.

### 3.3 Gas component effect analysis

The effect of the gas component on Hg<sup>0</sup> oxidation over Ag-Ce-Ti is shown in Fig. 6. The catalytic efficiency was high in the presence of HCl, which increases as the temperature

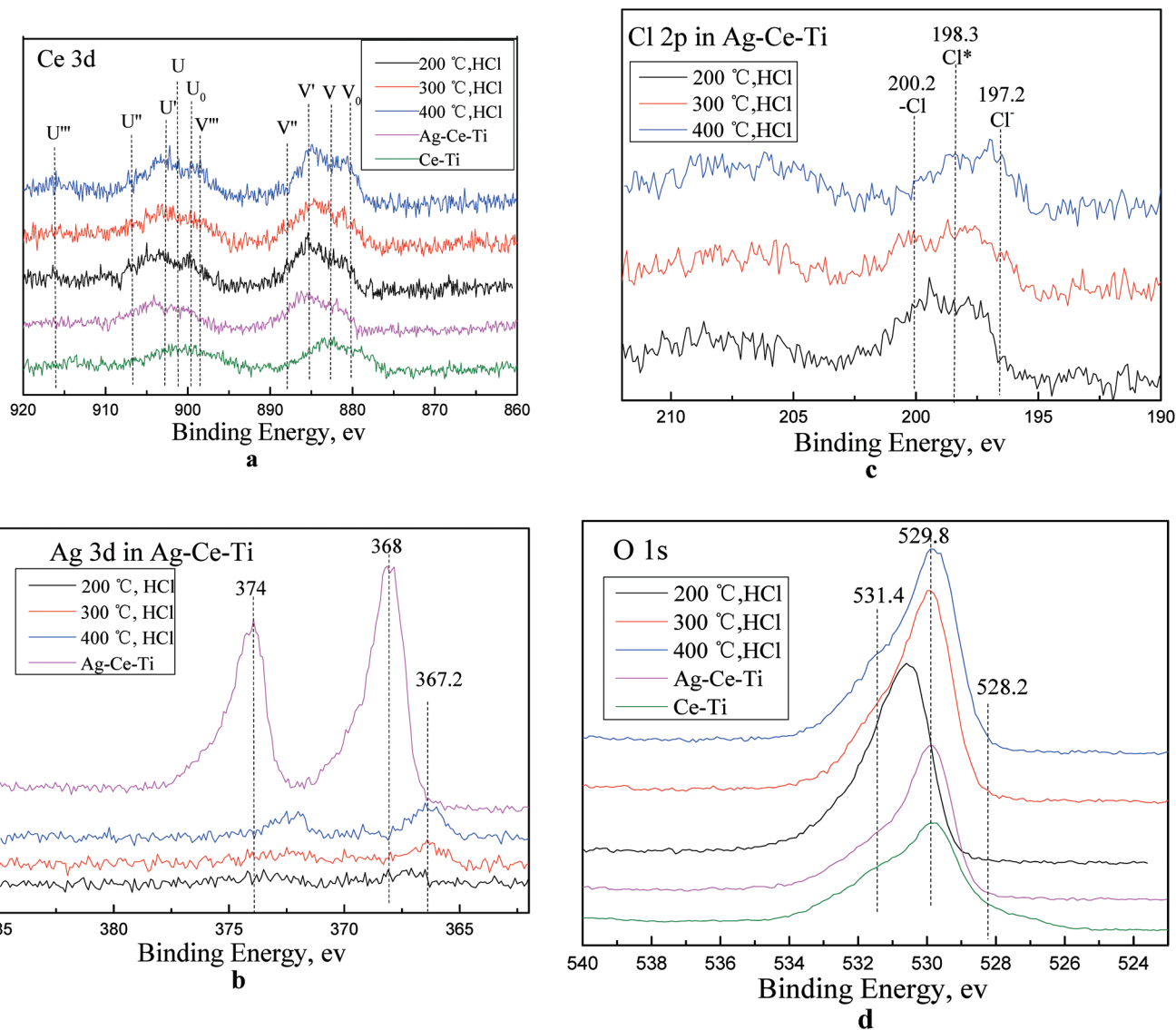


Fig. 4 XPS spectra of Ce-Ti, Ag-Ce-Ti and Ag-Ce-Ti passed with 15 ppm HCl at various temperatures: Ce 3d (a), Ag 3d (b), Cl 2p (c) and O 1s (d).

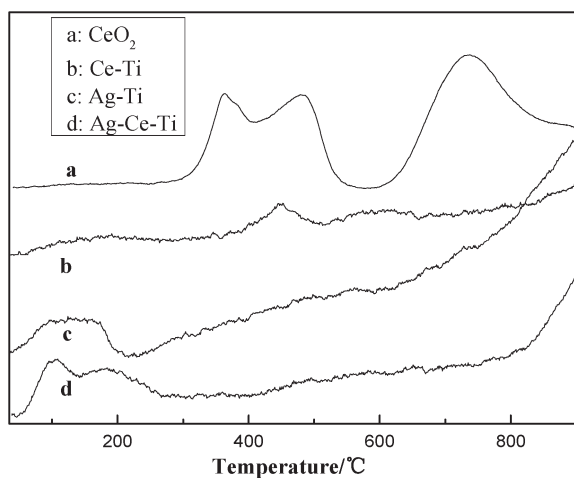


Fig. 5 TPR profiles of the various catalysts: CeO<sub>2</sub> (a), Ce-Ti (b), (c) Ag-Ti and Ag-Ce-Ti (d).

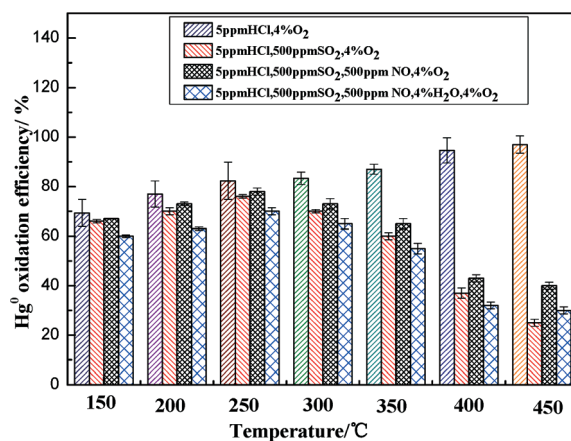


Fig. 6 The effect of gas component on Hg<sup>0</sup> oxidation over Ag-Ce-Ti.

increases. It indicated that HCl was the main catalytic component. When SO<sub>2</sub> was added, the Hg<sup>0</sup> oxidation efficiency began to decrease slightly at low temperature, while it dropped sharply at high temperature, suggesting that Ag–Ce–Ti showed superior resistance toward SO<sub>2</sub> at low temperature, and SO<sub>2</sub> might compete for the active sites to inhibit the reaction of Hg<sup>0</sup> and Cl at high temperature. The Hg<sup>0</sup> oxidation efficiency improved when NO was added, manifesting that NO promoted the Hg<sup>0</sup> oxidation. Besides, water inhibited the Hg<sup>0</sup> oxidation both at low temperature and high temperature.

### 3.4 Analysis of the mechanism of catalytic oxidation of Hg<sup>0</sup>

To clarify the catalytic mechanism of elemental mercury conversion over Ag–Ce–Ti, HCl and Hg<sup>0</sup> breakthrough experiments were conducted.

Fig. 7(a) shows the HCl breakthrough curves of Ag–Ce–Ti at various temperatures. Fig. 7(a) shows that HCl could be adsorbed on the surface of Ag–Ce–Ti, either at low temperatures or at high temperatures, and the adsorption ability of

HCl was reduced with the increase in temperature. The same trend can be seen in Fig. 7(b), which shows the Hg<sup>0</sup> breakthrough curves. The adsorption ability of Hg<sup>0</sup> was a little above 300 °C, indicating that Hg<sup>0</sup> was hardly adsorbed at high temperatures. It could be concluded that Hg<sup>0</sup> oxidation over the Ag–Ce–Ti catalyst probably occurred through the reaction of adsorbed HCl with adsorbed Hg<sup>0</sup> at low temperatures, the process of which follows the Langmuir–Hinshelwood mechanism.<sup>9</sup> Furthermore, at high temperatures, Hg<sup>0</sup> oxidation proceeded through the reaction of gas-phase or weakly adsorbed Hg<sup>0</sup> with adsorbed HCl *via* the Eley–Rideal mechanism.<sup>30</sup>

Fig. 8 shows the Hg<sup>0</sup> breakthrough curves over HCl pretreated Ag–Ce–Ti and Ce–Ti. Fig. 8(a) shows that the catalysts still exhibited oxidation ability even when HCl was not passed. This indicates that the chlorine species were adsorbed on Ag–Ce–Ti and participated in the reaction. The Hg<sup>0</sup> oxidation efficiency had a tendency to increase first and then slightly decrease with an increase in temperature, and was most effective at 300 °C. Because the catalysts were purged with nitrogen after pretreatment of HCl, there was hardly any Cl<sub>2</sub> adsorbed on the catalysts. The adsorption ability of HCl reduced with the increase in temperature referred

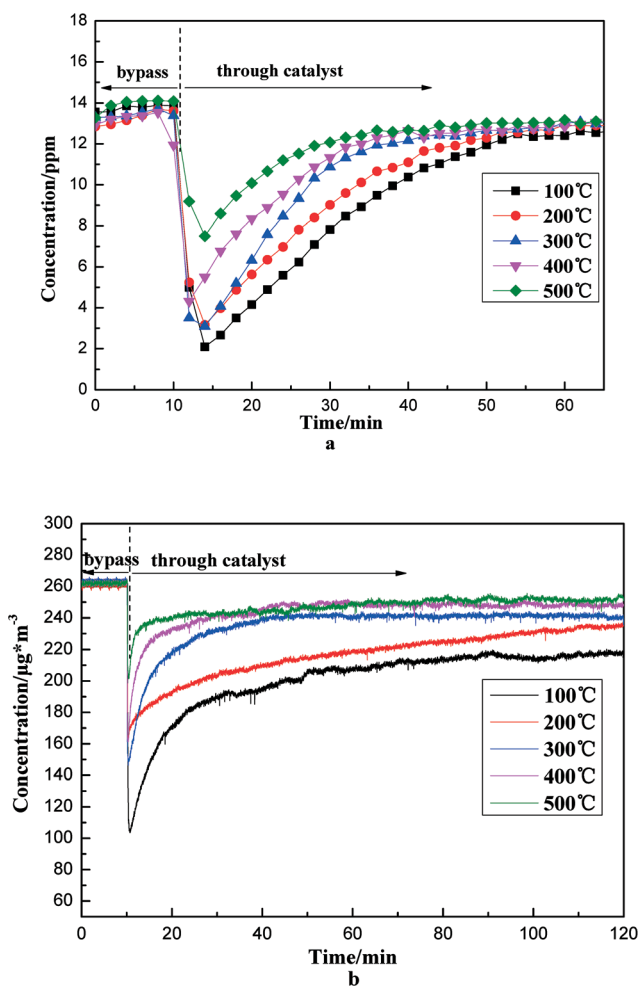


Fig. 7 HCl and Hg<sup>0</sup> breakthrough curves of Ag–Ce–Ti at various temperatures: HCl breakthrough curves (a) and Hg<sup>0</sup> breakthrough curves (b).

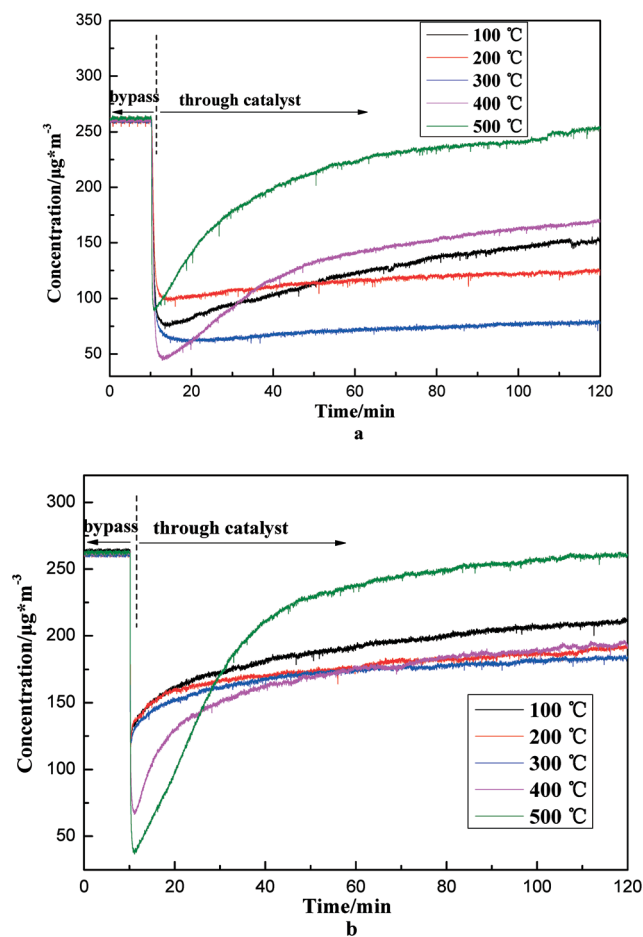


Fig. 8 Hg<sup>0</sup> breakthrough curves over HCl pretreated Ag–Ce–Ti and Ce–Ti: Ag–Ce–Ti (a) and Ce–Ti (b).

to in Fig. 7(a), so that the adsorbed component on the surface of the catalysts used for oxidizing  $\text{Hg}^0$  could be the active chlorine species formed by the reaction between adsorbed HCl and Ag–Ce–Ti, which could react with  $\text{Hg}^0$ . The amount of active chlorine species would increase at high temperatures due to the high catalytic ability of Ag–Ce–Ti. However, the amount of adsorbed HCl decreased at high temperatures, so the amount of adsorbed active Cl was highest at 300 °C, at which the  $\text{Hg}^0$  oxidation efficiency was the highest. When the temperature was higher than 300 °C, the  $\text{Hg}^0$  oxidation efficiency of Ag–Ce–Ti was low, which indicated that there was a little amount of active Cl adsorbed on the surface of catalysts. The improvement of the catalytic efficiency of Ag–Ce–Ti with the increase in temperature, which was referred to in Fig. 1, might be caused by the  $\text{Cl}_2$  generated by the reaction of active Cl which further reacted with  $\text{Hg}^0$  at high temperature.

Fig. 8(b) shows the  $\text{Hg}^0$  breakthrough curves over HCl pretreated Ce–Ti. It shows the same trend as Fig. 8(a). However, the  $\text{Hg}^0$  concentration increased with time and was higher than that of Ag–Ce–Ti, which indicated that the adsorbed active chlorine species was low due to the poor catalytic ability. It revealed that the active chlorine species was mainly adsorbed on silver nanoparticles, in agreement with the results of XPS analysis. Silver was important for the improvement of the catalytic ability.

To verify the role of chlorine, an experiment using  $\text{Cl}_2$  produced by Deacon reaction was carried out. Fig. 9 shows the yield of  $\text{Cl}_2$  catalyzed by Ag–Ce–Ti after passing 5000 ppm HCl. As can be seen from Fig. 9, the characteristic peak of  $\text{Cl}_2$  was not found below 400 °C, indicating that  $\text{Cl}_2$  was difficult to generate at low temperature and chlorine existed in the form of active Cl. With the increase in temperature, the intensity of  $\text{Cl}_2$  characteristic peak started to increase, as manifested by the increase in the yield of  $\text{Cl}_2$ , which might be due to the more gaseous chlorine atoms or the chlorine atoms having higher activity and reacting with the nearby chlorine atoms on the support at high temperature. The analysis above proved that active Cl reacted with  $\text{Hg}^0$  at low

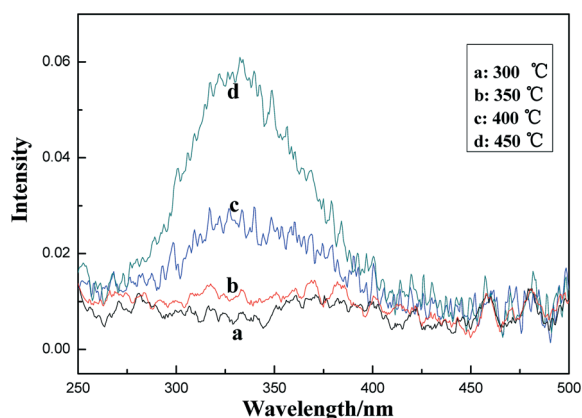


Fig. 9 The yield of  $\text{Cl}_2$  catalyzed by Ag–Ce–Ti after passing 5000 ppm HCl at different temperatures: 300 °C (a), 350 °C (b), 400 °C (c) and 450 °C (d).

temperature, and active Cl and  $\text{Cl}_2$  reacted with  $\text{Hg}^0$  at high temperature.

To study the mercury combination properties of the catalysts,  $\text{Hg}^0$  adsorption and desorption experiments were performed. Fig. 10 shows the Hg-TPD curves of the various catalysts after adsorption for 2 h. It can be seen from Fig. 10 that the adsorption ability of Ce–Ti was poor, which was indicated by the fact that  $\text{Hg}^0$  was less adsorbed on Ce(5%)–Ti in the process of the reaction. For Ag(5%)–Ti,  $\text{Hg}^0$  was desorbed as the temperature increased. This may be due to the decomposition of silver amalgam, indicating that silver was important for adsorption of  $\text{Hg}^0$ . The mercury combination ability of Ag(5%)–Ce(5%)–Ti was also strong, which is seen in Fig. 10. The desorption amount of  $\text{Hg}^0$  was similar to that of Ag(5%)–Ti, which manifested that  $\text{Hg}^0$  can be adsorbed on Ag(5%)–Ce(5%)–Ti at low temperatures and can react with the adsorbed HCl and active Cl, proving to have an excellent catalytic effect.

Based on the results above, the main reaction processes for  $\text{Hg}^0$  oxidation over Ag–Ce–Ti at low temperatures and high temperatures are shown in Fig. 11. The active chlorine species and  $\text{Hg}^0$  were both adsorbed on silver nanoparticles and reacted with each other at low temperatures following the Langmuir–Hinshelwood mechanism. At high temperatures, the active chlorine species adsorbed on silver nanoparticles and  $\text{Cl}_2$  reacted with the gas-phase or weakly adsorbed  $\text{Hg}^0$  via the Eley–Rideal mechanism and homogeneous gas-phase reaction. It further proved that the  $\text{Hg}^0$  oxidation ability could be enhanced by adding silver either at low temperatures or at high temperatures.

Fig. 12 shows the mercury concentration change curves over Ag–Ce–Ti after adding  $\text{O}_2$  and HCl at 150 and 350 °C as further proof of the results. Fig. 12 shows that the concentration of total mercury and elemental mercury both decreased after  $\text{O}_2$  was added either at low temperatures or at high temperatures, and the concentration of elemental mercury was lower than that of total mercury. It indicated that oxygen was important for  $\text{Hg}^0$  oxidation. In addition, a greater amount of  $\text{Hg}^{2+}$  was generated at high temperatures than at low temperatures, showing that the oxidation ability of Ag–Ce–Ti was

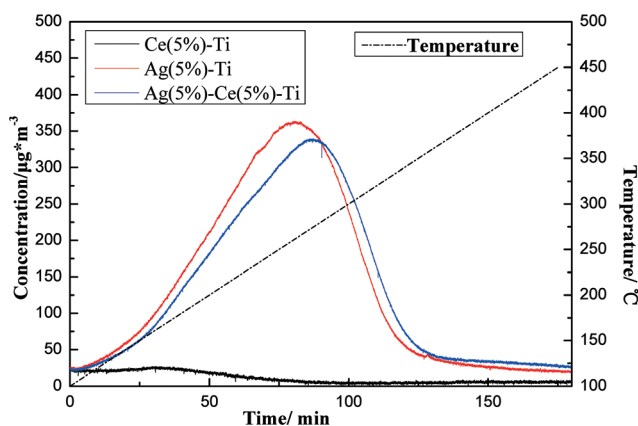


Fig. 10 Hg-TPD curves of various catalysts.

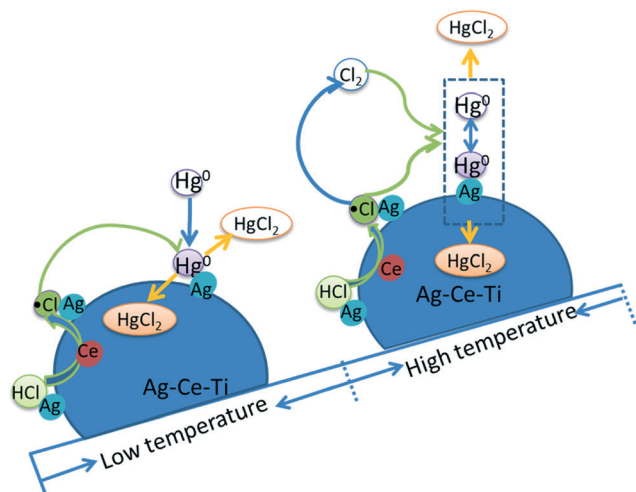


Fig. 11 The reaction process for  $\text{Hg}^0$  oxidation over Ag–Ce–Ti at low temperatures and high temperatures.

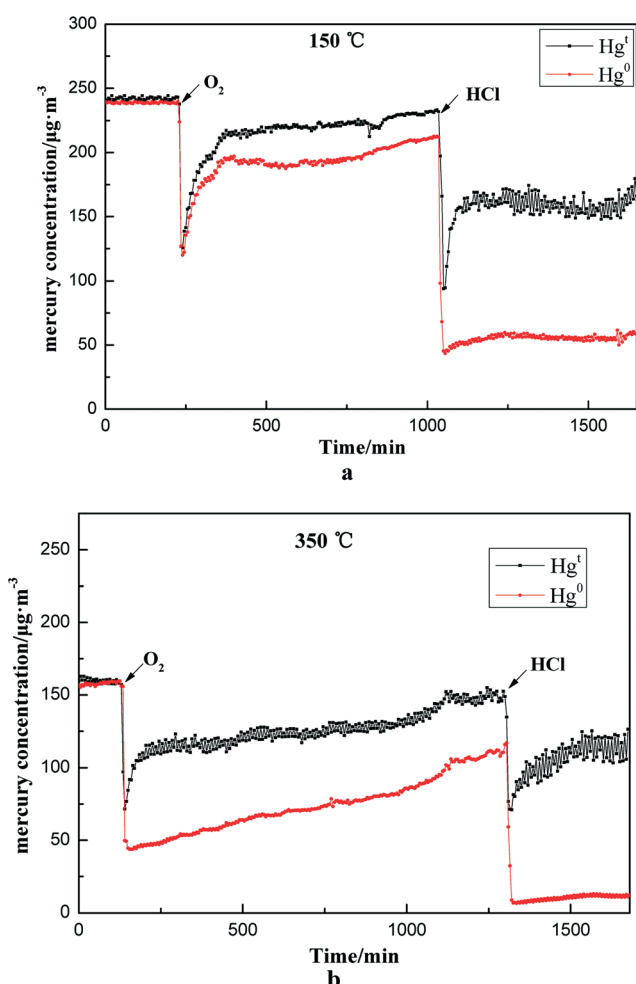


Fig. 12 Mercury concentration change curves over Ag–Ce–Ti after adding  $\text{O}_2$  and HCl at 150 °C and 350 °C: 150 °C (a) and 350 °C (b).

higher at high temperatures when oxygen existed. When HCl was added, the concentration of elemental mercury was further reduced both at 150 °C and 350 °C, and the gap

between  $\text{Hg}^0$  and  $\text{Hg}^{\text{I}}$  was larger, which indicated that HCl was the major catalytic component. The decrease in the concentration of  $\text{Hg}^0$  was due to the fact that  $\text{Hg}^0$  reacted with the adsorbed active Cl species and chlorine to produce  $\text{HgCl}_2$ . The concentration of total mercury was also reduced, which may have caused a small amount of  $\text{HgCl}_2$  to be adsorbed onto the catalyst.

## 4. Conclusions

Doping with silver can significantly improve the performance of the Ce–Ti catalyst at various temperatures. The characterization results indicated that silver nanoparticles were deposited on titania and the catalysts had better crystallization after addition of silver. Silver existed mostly in its metallic state and it can keep Ce in a greater amount of Ce(IV) states. HCl was oxidized to active Cl by  $\text{CeO}_2$  and then was adsorbed on the silver nanoparticles. Gas component analysis indicated that  $\text{SO}_2$  and water inhibited slightly the  $\text{Hg}^0$  oxidation, and NO can promote this reaction. HCl and  $\text{Hg}^0$  breakthrough curves and the  $\text{Cl}_2$  yield experiment revealed that active chlorine species and  $\text{Hg}^0$  were both adsorbed on silver nanoparticles and reacted with each other at low temperatures following the Langmuir–Hinshelwood mechanism. At high temperatures, active chlorine species adsorbed on silver nanoparticles and chlorine reacted with the gas-phase or weakly adsorbed  $\text{Hg}^0$  via the Eley–Rideal mechanism and homogeneous gas-phase reaction. These results proved that the  $\text{Hg}^0$  oxidation ability could be enhanced by addition of silver either at low temperatures or at high temperatures. Furthermore, the  $\text{Hg}^0$  adsorption and desorption experiments showed that the mercury combination ability of Ce(5%)–Ti was enhanced by addition of silver. Finally, the valence state change of mercury was analyzed and it was shown that HCl was the major catalytic oxidization component.

## Acknowledgements

This study was supported by the Major State Basic Research Development Program of China (973 program, no. 2013CB430005), the National Natural Science Foundation of China (no. 21277088, 50908145) and the National High-Tech R&D Program (863) of China (no. 2013AA065403, 2012AA062504).

## References

- 1 H. Yang, W. Hou, H. Zhang and L. Zhou, *Int. J. Environ. Sci. Technol.*, 2013, **10**, 689–696.
- 2 The US Environmental Protection Agency (EPA), *Final Mercury and Air Toxics Standards (MATS) for Power Plants*, <http://www.epa.gov/airquality/powerplanttoxics/actions.html>.
- 3 J. Dong, Z. H. Xu and S. M. Kuznicki, *Environ. Sci. Technol.*, 2009, **43**, 3266–3271.
- 4 Y. Li, M. Daukoru, A. Suriyawong and P. Biswas, *Energy Fuels*, 2009, **23**, 236–243.
- 5 N. Q. Yan, W. M. Chen, J. Chen, Z. Qu, Y. F. Guo, S. J. Yang and J. P. Jia, *Environ. Sci. Technol.*, 2011, **45**, 5725–5730.

- 6 Y. Liu, Y. J. Wang, H. Q. Wang and Z. B. Wu, *Catal. Commun.*, 2011, **12**, 1291–1294.
- 7 J. F. Li, N. Q. Yan, Z. Qu, S. H. Qiao, S. J. Yang, Y. F. Guo, P. Liu and J. P. Jia, *Environ. Sci. Technol.*, 2010, **44**, 426–431.
- 8 W. J. Lee and G. N. Bae, *Environ. Sci. Technol.*, 2009, **43**, 1522–1527.
- 9 H. Li, C.-Y. Wu, Y. Li and J. Zhang, *Environ. Sci. Technol.*, 2011, **45**, 7394–7400.
- 10 H. L. Li, C. Y. Wu, L. Q. Li, Y. Li, Y. C. Zhao and J. Y. Zhang, *Fuel*, 2013, **113**, 726–732.
- 11 C. W. Lee, S. D. Serre, Y. Zhao, S. J. Lee and T. W. Hastings, *J. Air Waste Manage. Assoc.*, 2008, **58**, 484–493.
- 12 T. Kou, D. Li, C. Zhang, Z. Zhang and H. Yang, *J. Mol. Catal. A: Chem.*, 2014, **382**, 55–63.
- 13 X. Yang, F. Ma, K. Li, Y. Guo, J. Hu, W. Li, M. Huo and Y. Guo, *J. Hazard. Mater.*, 2010, **175**, 429–438.
- 14 R. Delaigle, P. Eloy and E. M. Gaigneaux, *Catal. Today*, 2011, **175**, 177–182.
- 15 L. Ma, D. Wang, J. Li, B. Bai, L. Fu and Y. Li, *Appl. Catal., B*, 2014, **148**, 36–43.
- 16 B. M. Reddy, A. Khan, P. Lakshmanan, M. Aouine, S. Loridant and J.-C. Volta, *J. Phys. Chem. B*, 2005, **109**, 3355–3363.
- 17 H. Li, J. Li and Y. Huo, *J. Phys. Chem. B*, 2006, **110**, 1559–1565.
- 18 B. Xin, L. Jing, Z. Ren, B. Wang and H. Fu, *J. Phys. Chem. B*, 2005, **109**, 2805–2809.
- 19 M. Wen, L. Zhou, W. Guan, Y. Li and J. Zhang, *Appl. Surf. Sci.*, 2010, **256**, 4226–4230.
- 20 C. Hu, Y. Lan, J. Qu, X. Hu and A. Wang, *J. Phys. Chem. B*, 2006, **110**, 4066–4072.
- 21 E. Beche, P. Charvin, D. Perarnau, S. Abanades and G. Flamant, *Surf. Interface Anal.*, 2008, **40**, 264–267.
- 22 S. B. Atla, C.-C. Chen, C.-Y. Chen, P.-Y. Lin, W. Pan, K.-C. Cheng, Y. M. Huang, Y.-F. Chang and J.-S. Jean, *J. Photochem. Photobiol., A*, 2012, **236**, 1–8.
- 23 P. M. Carrasco, M. Cortazar, E. Ochoteco, E. Calahorra and J. A. Pomposo, *Surf. Interface Anal.*, 2007, **39**, 26–32.
- 24 H. Piao, K. Adib and M. A. Barteau, *Surf. Sci.*, 2004, **557**, 13–20.
- 25 V. V. Kaichev, V. I. Bukhtiyarov, M. Havecker, A. Knop-Gercke, R. W. Mayer and R. Schlogl, *Kinet. Catal.*, 2003, **44**, 432–440.
- 26 S. Watanabe, X. L. Ma and C. S. Song, *J. Phys. Chem. C*, 2009, **113**, 14249–14257.
- 27 P. Li, Y. Xin, Q. Li, Z. P. Wang, Z. L. Zhang and L. R. Zheng, *Environ. Sci. Technol.*, 2012, **46**, 9600–9605.
- 28 S. Zhao, Y. Ma, Z. Qu, N. Yan, Z. Li, J. Xie and W. Chen, *Catal. Sci. Technol.*, 2014, **4**, 4036–4044.
- 29 Y. Kang, M. Sun and A. Li, *Catal. Lett.*, 2012, **142**, 1498–1504.
- 30 W. Gao, Q. C. Liu, C. Y. Wu, H. L. Li, Y. Li, J. Yang and G. F. Wu, *Chem. Eng. J.*, 2013, **220**, 53–60.